Digital Image Processing of Earth Observation Sensor Data

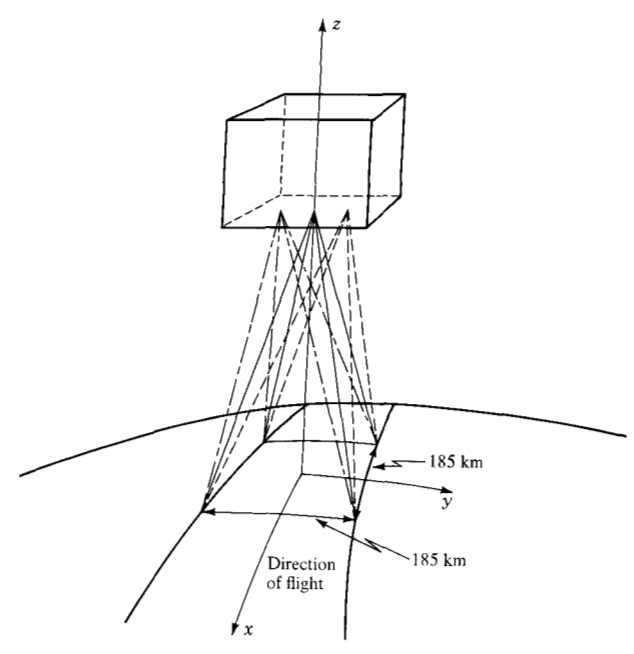
Abstract: This paper describes digital image processing techniques that were developed to precisely correct Landsat multispectral Earth observation data and gives illustrations of the results achieved, e.g., geometric corrections with an error of less than one picture element, a relative error of one-fourth picture element, and no radiometric error effect. Techniques for enhancing the sensor data, digitally mosaicking multiple scenes, and extracting information are also illustrated.

Introduction

Landsat

In July 1972 the U.S. National Aeronautics and Space Administration (NASA) launched the first Earth Resources Technology Satellite (ERTS-1), recently renamed "Landsat-1," and a second satellite was launched in January 1975. A number of significant scientific discoveries and practical benefits have already resulted [1-8]; see Table 1 for the major disciplines and applications of the Landsat program.

Figure 1 Return Beam Vidicon (RBV) camera and its field of view.



Each unmanned Landsat makes 14 orbits per day, viewing 185-km-wide strips of the Earth [9]. Each satellite provides global coverage once every 18 days, so that the two satellites provide such coverage every nine days. All equatorial crossings occur at approximately the same *local* time each day, 9:30 a.m.; this holds for all parts of the world. The satellite orbit plane precesses at about one degree per day and the sun-synchronous orbit has a constant orbit-plane angle relative to the sun-Earth line, which minimizes misinterpretation of satellite-sensor data due to shadow effects from the sun. The physical parameters of the Landsat mission are summarized in Table 2.

Landsat carries two kinds of sensors to detect and record sunlight reflected from the Earth's surface in particular spectral bands [9]:

The Return Beam Vidicon (RBV) is a three-band, three-camera television system (Fig. 1-) using conventional lenses and shutters, and vidicons for image scanning and storing prior to transmission of the image data to ground stations. The cameras are sensitive to scene radiance in wavelengths from 0.48 to 0.83 μ m. Their field of view is an area 185 km \times 185 km.

The Multispectral Scanner (MSS) consists of an oscillating mirror and an optical system which reflect and direct scene radiance into a solid-state detector array that is sensitive to wavelengths in four spectral bands between 0.5 and 1.1 μ m (not including thermally generated radiation); see Fig. 2. Six scan lines are simultaneously swept in each spectral band with one mirror oscillation. The detectors subtend an instantaneous field of

Table 1 Landsat (ERTS) data and applications.

Agriculture, Forestry, Range	Crop census Crop yield Identification of vegetation disease Land use inventory
Oceanography, Marine resources	Fish production Ship routing Sea state and ice conditions
Hydrology	Water resources inventory Fresh-water source identification Flood monitoring Health monitoring of lakes Pollution monitoring
Geology	Tectonic feature identification Geologic and physiographic mapping Mineral and field exploration Earthquake-area studies Temporal studies (glaciers, volcanos, shoreline erosion)
Geography	Thematic maps of land use Physical geography (to improve land use)

view on the ground 79 m on a side; their outputs are in digital form for transmission to ground stations. Characteristics of the Multispectral Scanner are listed in Table 3.

• Digital image processing concepts

Earth observation data acquired by on-board spacecraft sensors are affected by a number of electronic, geometric, mechanical, and radiometric distortions that, if left uncorrected, would diminish the accuracy of the information extracted and thereby reduce the utility of the data.

Previous methods of correction, using electro-optical processing techniques, have had some limitations [9]. Recent investigations [10-12] have shown the superiority of a digital approach over that of electro-optics as a consequence of the former's processing flexibility, fewer required data conversions, and improved accuracy and quality of the information developed.

To correct sensor data, internal and external errors must be determined—they must be either predictable or measurable. Internal errors are due to sensor effects; they are systematic or stationary, i.e., constant (for all practical purposes), and can be determined from prelaunch calibration measurements. External errors are due to platform perturbations and scene characteristics, which are variable in nature but can be determined from ground control and tracking data. Thus, the information required for correcting data distortion can be obtained (within certain limits of precision). Figure 3 presents a simplified illustration of the sequence of sensor-data processing from acquisition to application.

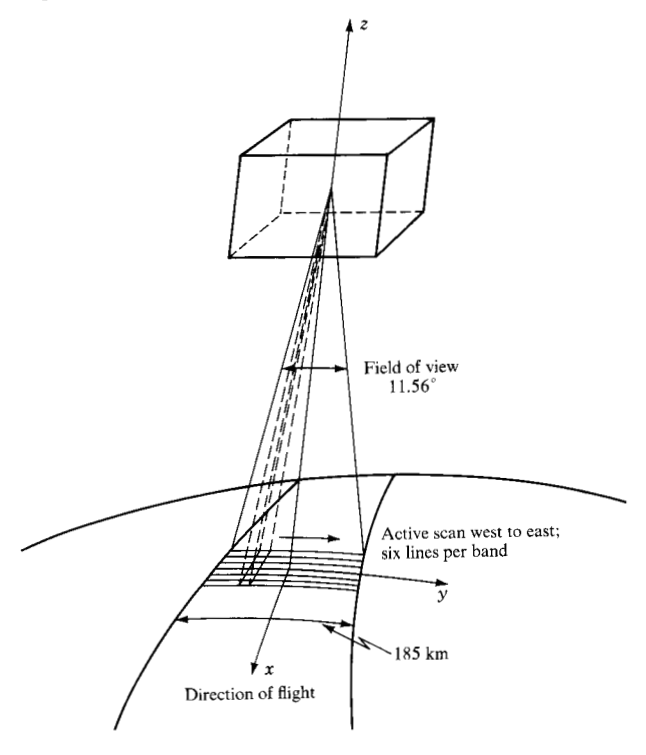
Table 2 Landsat (ERTS) mission parameters.

Apogee	917 km
Perigee	898 km
Semi-major axis	7285.7 km
Inclination	99.0 degrees
Anomalistic period	103 minutes
Eccentricity	0.0012
Local time at descending node	
(equatorial crossing)	9:30
Coverage cycle duration	18 days
Distance between adjacent ground tracks	159.38 km
• •	

Table 3 Multispectral Scanner (MSS) characteristics.

Instantaneous field of view	0.086 mrad
Earth area subtended	6240 m ²
Mirror oscillation range	±2.89 degrees
Mirror oscillation frequency	13.62 Hz
Scan lines per oscillation	6
Cross track field of view	11.56 degrees
Cross track scan	185 km
Spectral band range: 4	0.5 to 0.6 μ m
5	0.6 to 0.7 μ m
6	0.7 to 0.8 μ m
7	0.8 to 1.1 μ m
Number of detectors	24
Sampling interval of detector output	9.95 µs
Sample word length	6 bits
Samples per line	3240
Lines per bands	2340
Information per band	7.6×10^6 bytes
Information per scene	30.4×10^6 bytes

Figure 2 Multispectral Scanner (MSS) and its field of view.



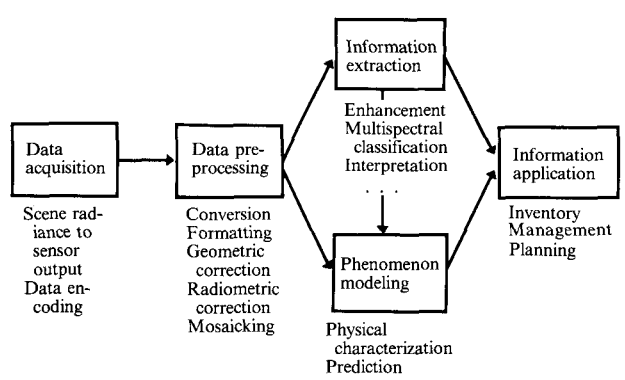


Figure 3 Simplified scheme of sensor-data processing stages.

The principal error sources (for the Multispectral Scanner) and the maximum compensation for the errors, as determined by statistical analysis, are the following:

Platform effects

Altitude Departures of the spacecraft from nominal altitude produce scale distortions in the sensor data. For the MSS, this distortion is along-scan only and varies with time; the magnitude of correction is 1.5 km.

Attitude Nominally, the sensor axis system is maintained with one axis normal to the Earth's surface and another parallel to the spacecraft velocity vector. As the sensor departs from this attitude, geometric distortion results. For the MSS, the complete attitude time-history must be known to compensate for the distortion; magnitude of correction: pitch, 12 km; roll, 12 km; yaw, 2.46 km; pitch rate, 0.93 km; roll rate, 0.54 km; and yaw rate, 0.040 km.

Scan-skew During the time required for the MSS mirror to complete an active scan, the spacecraft moves along the ground track. Thus, the ground swath scanned is not normal to the ground track but is slightly skewed, which produces cross-scan geometric distortion; the magnitude of correction is 0.082 km.

Velocity If the spacecraft velocity vector departs from nominal values, the ground track covered by a given number of successive mirror sweeps changes, producing along-track scale distortion; the magnitude of correction is 1.5 km.

Scene effects

Earth rotation As the MSS mirror completes successive scans, the Earth rotates beneath the sensor. Thus, there is a gradual westward shift of the ground swath being scanned. This causes along-scan distortion; the magnitude of correction is 13.3 km.

Map projection For Earth resources use, image data are usually required in a specific map projection. Although map projection does not constitute a geometric error, it does require a geometric transformation of the input data, and this can be accomplished by the same operations that compensate for distortion in the data; the magnitude of correction is 3.7 km along scan and along track (for the continental U.S.).

Sensor effect

Mirror sweep The MSS mirror scanning rate varies nonlinearly across a scan because of imperfections in the electromechanical driving mechanism. Since data samples are taken at regular intervals of time, the varying scan rate produces along-scan distortion; the magnitude of correction is 0.37 km.

Scene and sensor effects

Panorama The imaged ground area is proportional to the tangent of the scan angle rather than to the angle itself and, since data samples are taken at regular intervals, this produces along-scan distortion; the magnitude of correction is 0.12 km.

Perspective For most Earth resources applications, the desired Landsat images represent the projection of points on the Earth on a plane tangent to the Earth at the nadir, with all projection lines normal to the plane. The sensor data, however, represent perspective projections, i.e., projections whose lines meet at a point above the tangent plane. For the MSS, this produces only along-scan distortion; the magnitude of correction is 0.08 km.

Atmospheric effects

The scene radiance is dispersed and attenuated by the atmosphere between the sensor and the ground. Compensation for these effects is difficult but, if it can be done, increases the accuracy of information extraction still further. For example, see the discussion of sensor requirements by Kidd and Wolfe [13].

Elements of digital correction

The procedure developed for correction of satellite imagery is based on the computation of geometric coefficients from models that describe the distortion in the image. After obtaining these coefficients, a mapping function can be synthesized for geometric and radiometric correction of the sensor data. In this section we discuss the digital techniques that were developed to preprocess (correct) Earth observation data. These techniques have been applied to a variety of problems in addition to those used here as examples.

• Ground Control Points (GCPs)

Because tracking and spacecraft attitude data are not known precisely, Ground Control Points are used to obtain external reference information. A GCP is a physical feature detectable in a scene, whose location and elevation are known precisely. Typical GCPs are airports, highway intersections, land-water interfaces, geological and field patterns, etc. A registration operation is used to match a small image (subimage) area containing the GCP with a scene to be corrected, acquired possibly at a later time but containing the same feature.

Computationally efficient techniques have been developed to locate GCPs in digital data arrays. These are based on implementations [14, 15] of Sequential Similarity Detection Algorithms (SSDA), originally developed by Barnea and Silverman [14].

Sequential Similarity Detection Algorithms [14]

In this technique, also known as template matching, it is necessary to determine the similarity, or distance (in our case the difference in intensity), between two elements. A class of functions called metrics, which is a conventional abstraction of the notion of Euclidian distance, is used.

The principle of operation involves differencing an intensity-normalized random sample of corresponding points in the GCP and search areas and summing the absolute values of the differences. When the sum exceeds a selected threshold value, the subimages are considered to be dissimilar, the GCP area is displaced in relation to the search area, and another comparison is made. This process is repeated until a minimum sum function is found, which corresponds to the coordinates x, y of a best match between the GCP and the search area.

Consider two images, the search area S and the "window" (GCP subimage) W, illustrated in Fig. 4. The search area is an $L \times L$ array of digital picture elements which can assume one of G gray (intensity) levels. The window is an $M \times M$ (M < L) array of digital picture elements having the same gray-scale range. By superimposing the window on the search area, and by constraining the translation of the window so that at all times it is contained entirely within the search area, subimages $S_M^{i,j}$ are defined, which are $M \times M$ arrays of digital picture elements.

Each subimage is identified by the coordinates i, j of its upper left corner. Because of the constraint on the translation of the window (within S only), the domain of definition of the subimages—called the allowed range of reference points—is smaller than the search area.

The search for a point with coordinates i^* , j^* , in this domain, that indicate the position of the subimage which is most "similar" to the given window is called translational registration. For each point i, j there are M^2 points

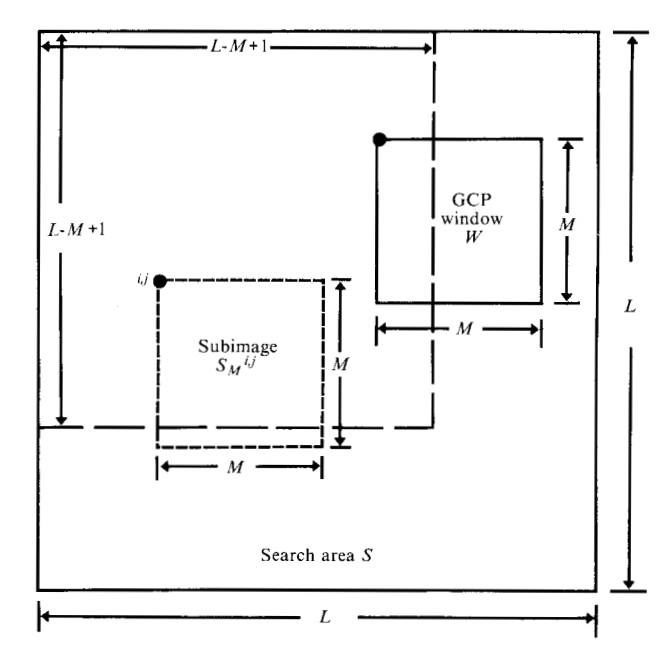


Figure 4 Illustration of the search area, allowed range of reference points, and the associated window.

of the subimage to be compared with the M^2 corresponding points of the window. Since there are $(L-M+1)^2$ points in the domain of definition, conventional correlation methods require comparison of $M^2(M-L+1)^2$ pairs of points. Barnea and Silverman used a Constant Threshold Algorithm, in which the pairs of points to be compared are selected in random order from a non-repeating sequence of integers, $1, 2, \dots, M^2$. The advantage of this technique relative to conventional correlation methods or the fast Fourier transform method is that few computations are performed when no similarity exists, which results in a decrease in registration time of about two orders of magnitude [14, 15].

The Sequential Similarity Detection Algorithms are usually used to get to the neighborhood of the best match. Then a 5×5 grid of correlation coefficients, centered at the best integral picture element (pixel) match, as determined by the SSDA, is computed. Next, a smooth surface is fitted to the grid and the Fletcher-Powell method [16] is used to attain sub-pixel GCP registration accuracy.

We define a *success ratio* as the number of correct registrations divided by the total number of registration attempts. The primary factor affecting the success ratio is the temporal and seasonal variation between the GCP and the scene to be processed. Table 4 shows that the registration success ratio is reasonably high, even for data separated in time by one year [12]. Another factor involves the spectral characteristics of the GCP feature.

For example, macadam airfields can be detected and registered more successfully in the infrared bands (6 and 7) than in the visible spectral bands (4 and 5). Generally, to increase reliability, redundant GCPs are processed.

Mapping operation

Spacecraft roll, pitch, and yaw data are not provided with sufficient accuracy by the satellite attitude determination system, and the ephemeris data do not provide either altitude or ground position with sufficient accuracy; these parameters must be calculated from knowledge of the GCP locations.

Differences between actual and observed GCP locations are used to evaluate the coefficients of cubic polynomial time functions of roll, pitch, and yaw, and of a linear time function of altitude deviation [12]. The GCPs are first located in the input image (sensor data) and then mapped into the Earth tangent plane using models based on all those errors that can be predicted or determined from tracking data. The tangent plane projection contains a Cartesian coordinate system with its origin at the center of the image and the x-y plane tangent to the Earth ellipsoid at this origin. The positive x axis is in the direction of the nominal spacecraft ground track; the z axis is oriented away from the center of the Earth; and the y axis completes a right-handed coordinate system. The functional steps that generate the mapping function are summarized in Fig. 5.

• Geometric correction function

The input image is an array of digital data which represents a geometrically distorted, one-dimensional perspective projection of some portion of the Earth's surface. The output image is a geometrically corrected map projection of the same ground area.

A network of grid points spanning the output image area is mapped into the input image using a pair of bivariate polynomials; the following mapping functions [12, 17] provide this transformation:

$$v = v(x, y) = \sum_{p=0}^{N} \sum_{q=0}^{N-p} a_{pq} x^{p} y^{q};$$

$$u = u(x, y) = \sum_{p=0}^{N} \sum_{q=0}^{N-p} b_{pq} x^{p} y^{q}.$$

Rather than apply the mapping functions to all points of the output image, an interpolation grid is established on the output image. The grid is constructed so that if the four corner points of any grid mesh are mapped with the aid of the mapping function polynomials, all points internal to the mesh can be located in the input image, with sufficient accuracy, by bilinear interpolation from the corner points.

After determining the position of an output picture element on the input image, several methods can be used to calculate the intensity value of the output element. For example:

Table 4 Registration success ratios as a function of the temporal separation between the acquistion of search area and window area data (Chesapeake Bay vicinity).

		Success ratio							
Surface feature	Separation (days)	Band 4	Band 5	Band 6	Band 7				
Large land-water interfaces	18	0.40	0.33	0.93	1.00				
	108	0.36	0.36	0.57	0.57				
	288	0.79	0.64	1.00	0.93				
	378	0.64	0.71	1.00	1.00				
Small land-water interfaces	18	0.71	0.57	1.00	1.00				
	108	0.86	0.71	0.71	0.43				
	288	0.67	0.67	0.33	0.33				
	378	0.86	0.71	0.86	0.71				
Interstate-grade highways	18	1.00	1.00	0.94	0.94				
	108	1.00	1.00	0.63	0.38				
	288	0.88	1.00	0.63	0.44				
	378	0.88	0.88	0.75	0.88				
Airfields (macadam)	18	0.00	0.00	1.00	1.00				
	108	1.00	1.00	1.00	1.00				
	288	1.00	1.00	1.00	1.00				
	378	1.00	1.00	1.00	1.00				
Airfields (concrete)	18	1.00	1.00	1.00	1.00				
· •	108	0.00	1.00	1.00	0.00				
	288	0.00	1.00	0.00	0.00				
	378	1.00	1.00	1.00	1.00				

The *nearest-neighbor* method, which selects the intensity of the closest input element and assigns that value to the output element:

$$I(x, y) = I(u, v)$$
.

The *bilinear interpolation* method, which uses four neighboring input values to compute the output intensity by two-dimensional interpolation:

$$I(x, y) = a_1 I(u, v + 1) + a_2 I(u, v) + a_3 I(v + 1, v + 1)$$
$$+ a_4 I(u + 1, v).$$

The cubic convolution method [11, 12, 18], originally suggested by Rifman and McKinnon, which uses 16 neighboring values to compute the output intensity (see the Appendix):

$$I(x, y) = \sum_{m,n} a_{m,n} I(u + m, v + n), -1 \le m, n \le 2.$$

Resampling of MSS image data can be used to eliminate spatial discontinuities due to nonsimultaneous detector sampling and geometric image correction operations.

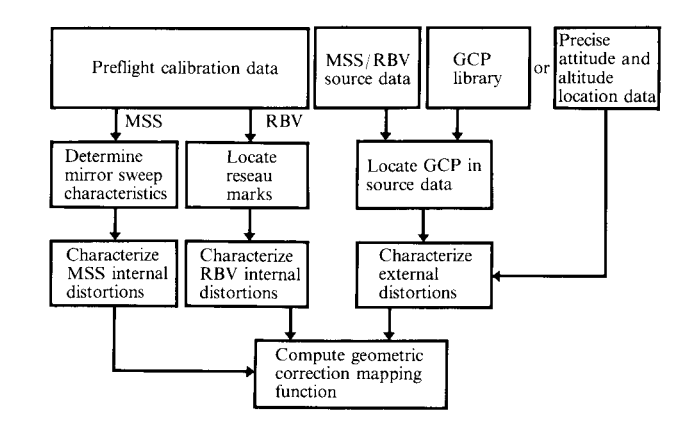
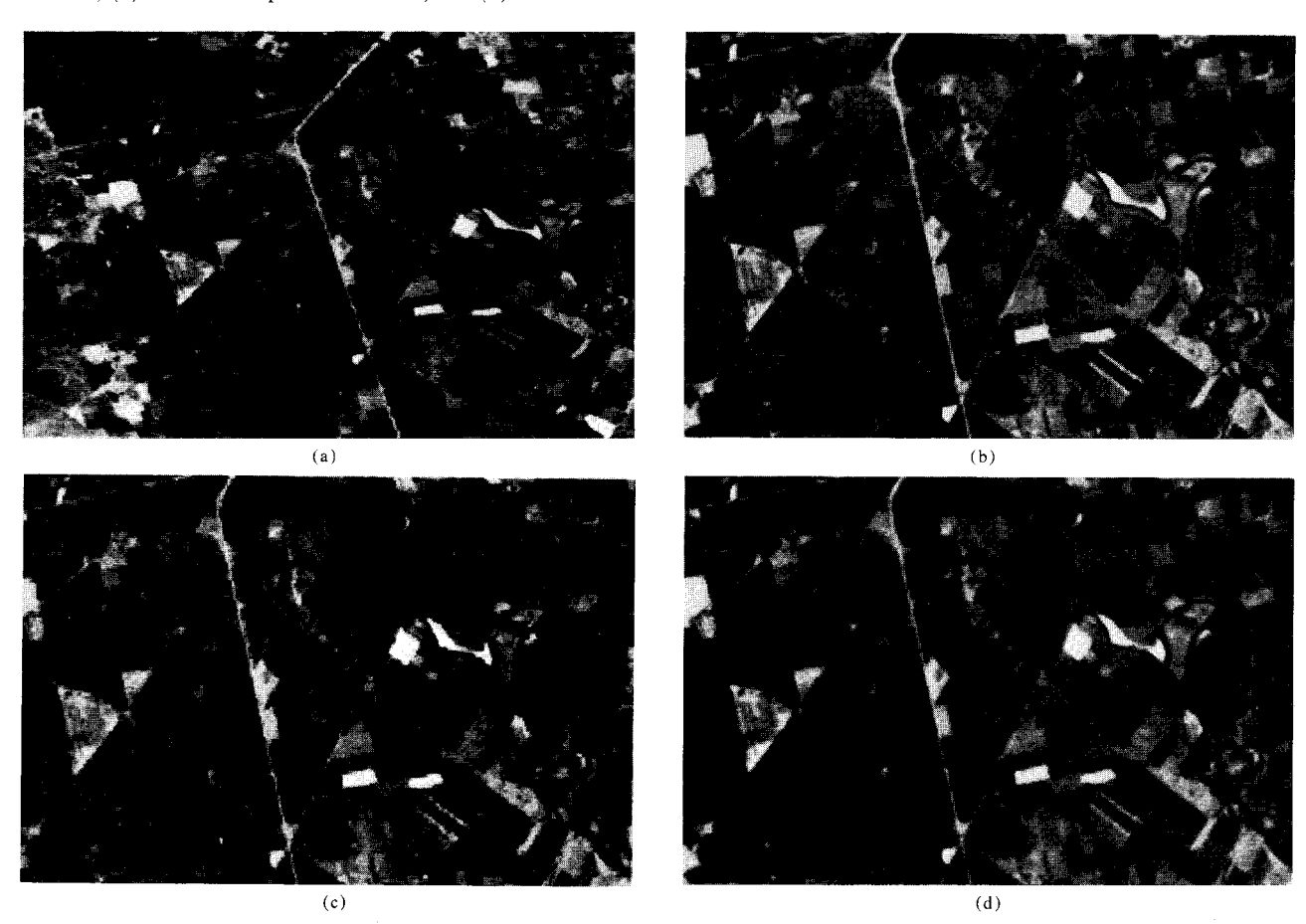


Figure 5 Functional steps for the generation of the mapping functions.

Figure 6 shows an MSS subimage, extracted from a central California scene (Fig. 8), before and after use of the three resampling algorithms [12]. Discontinuities in the input data have been eliminated by the bilinear interpolation and cubic convolution methods. Some high-frequency loss, due to low-pass filtering of the image data, can be noted in the corrected image for which bilinear interpolation was used.

Figure 6 MSS subimage area (band 5) before and after application of resampling algorithms: (a) original data; (b) nearest-neighbor method; (c) bilinear interpolation method; and (d) cubic convolution method.



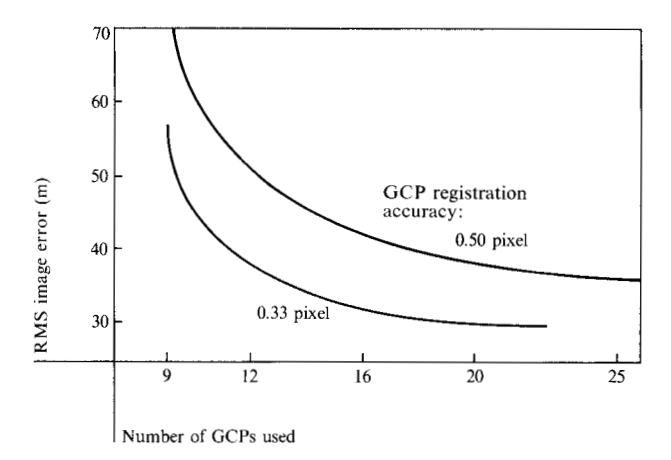


Figure 7 Root-mean-square (RMS) distance error as a function of the number and registration accuracy of the GCPs used.

Table 5 Truncated radiometric correction table (for three-bit data).

Detector output	Corrected value R for function ^a							
V	1	2	3	4				
000	000	000	000	000				
001	000	001	000	000				
010	000	011	000	001				
100	010	110	010	100				
011	001	100	010	100				
101	011	111	100	110				
110	100	111	110	111				
111	101	111	111	111				

^aFunctions: 1) R = V - 2; 2) R = 1.5V; 3) R = 2(V - 3); and 4) R = 0 if $V \le 1$, R = 1.5(V - 1) if 1 < V < 6, and R = 7 if $V \ge 6$.

Table 6 Geometric MSS error analysis (ninety percent of the GCPs have errors less than that indicated).

Scene	Number of GCPs	Relative geometric accuracy (m)		
Chesapeake Bay ^a	16	72		
Monterey Bay ^b	14	80		
Chesapeake Bay ^a Monterey Bay ^b New Jersey ^c	15	80		
New Jersey ^c	16	79		

[&]quot;Area in Fig. 11.

Table 7 RBV error analysis and radiometric correction zones.^a

Band	Number of GCPs	RMS error (m)	Maximum error (m)	Number of horizontal fields	Number of vertical fields	Total zones
1	9	37.1	64.9	191	138	26 358
2	9	36.3	53.2	184	119	21 896
3	8	42.1	68.0	181	106	19 186

^aData relate to Figs, 8(f) and (g).

Figure 8 (facing page) Digitally processed images of a central California area: (a) MSS image (band 7) before and (b) after geometric correction (see the data in Table 6); (c) MSS image (band 7) before radiometric enhancement, (d) subimage after radiometric road network enhancement, and (e) subimage after radiometric water pattern enhancement; (f) RBV image (band 2) before and (g) after radiometric correction (see the data in Table 7).

• Radiometric correction

Multispectral Scanner

The MSS has 24 solid-state detectors, six for each band. Both bias and gain errors can exist with uncalibrated detector data. Each detector voltage output is digitized into 64 values, or counts. An internal MSS calibration lamp is scanned by the detectors and the data are used to provide absolute (in terms of the lamp strength) and relative (in terms of each detector) response information. The corrections thus generated are implemented by simple table-lookup operations; see Table 5 for an example of radiometric corrections. The detector output (V)is used as an address or pointer to the correct value in the table, and the table value (R) is used as the corrected image-element radiance response. In Table 5 the response of Function 1 shows bias error compensation; Function 2, gain error compensation with rounding and truncation; Function 3, bias and gain compensation; and Function 4, nonlinear compensation. Highly nonlinear compensation and enhancement transformations can be implemented in the same manner.

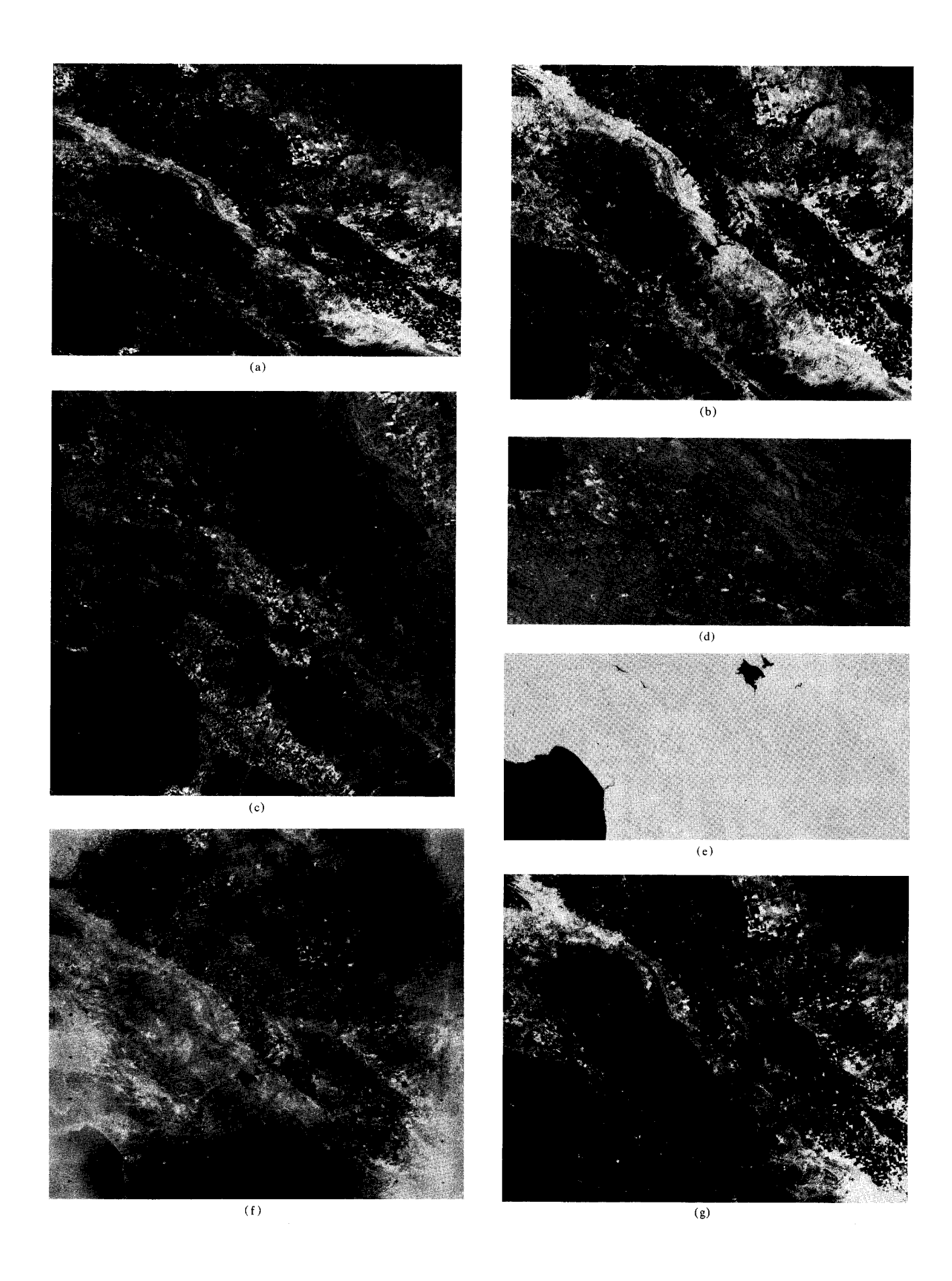
Return Beam Vidicon

The RBV computer-compatible tapes contain image data that have been sampled and digitized with six-bit quantization. Thus, there are 64 possible input values. If a table which specifies the correct output intensity for each of the 64 input intensities can be defined, radiometric correction of the RBV images can also be accomplished by table-lookup operations. This is essentially the technique used, but it is complicated by the fact that RBV radiometric errors vary across the image; this results in the need to use multiple correction tables.

The RBV data suffer from significant shading (non-uniform response) effects. Since the objective of RBV

46

Area in Figs. 8 and 15.
Areas in Fig. 11.



47

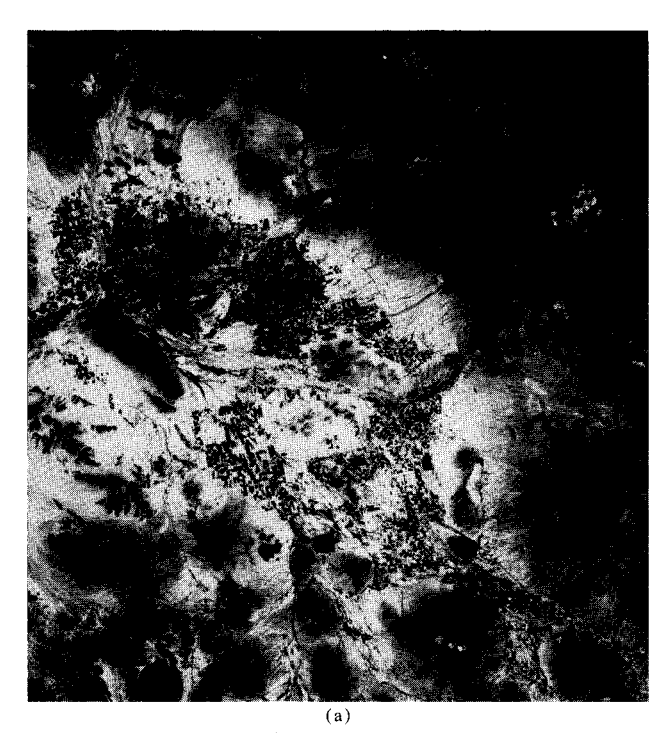




Figure 9 MSS scenes of the Phoenix, Arizona area geometrically corrected to be in registration; (a) acquired on October 16, 1972 and (b) acquired on November 21, 1972.

Figure 10 Subimage of a digital mosaic of two MSS scenes showing a circular geologic feature.



correction is to modify the image data intensity to compensate for the spatially variable response characteristics, a method has been developed that mathematically structures the RBV image into correction zones. (A sufficient number of such zones must be established to have a nearly continuous radiometric response function.) Each zone has a unique radiometric correction table to be used for compensation of the RBV errors. In effect, RBV radiometric correction is performed in two stages: generation of the correction tables (an off-line operation) and then application of the correction.

Pre-flight calibration readings at several intensity levels from a uniform light source provide an 18×18 array of points in the RBV image. These readings, in terms of voltage ranging from 0.32 to 1.10 V, are then scaled to the digital range 0 to 63. From these uniform input values, 18×18 arrays of gain (G) and bias (B) are computed for the correction equation, $V_{\rm out}=G(V_{\rm in}+B)$.

These input readings are distributed uniformly throughout the image but do not include the edges. Various extrapolation techniques, with polynomial functions up to third order, were tested for use in estimating the



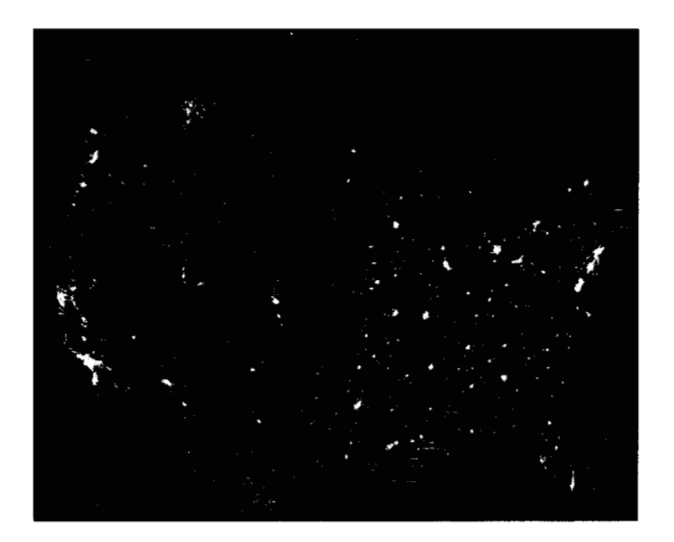
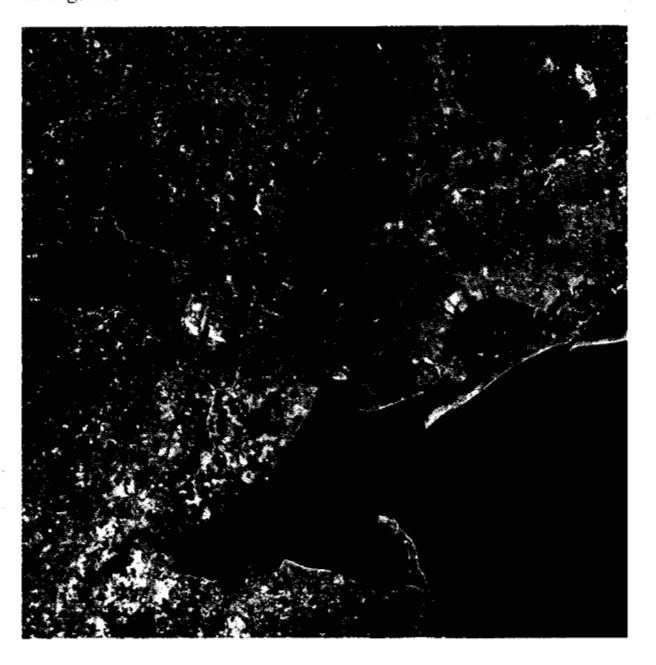


Figure 12 Digital mosaic of the United States produced from visible and infrared radiation recorded at night.

Figure 11 (at left) Digital mosaic color composite (bands 4, 5, and 7) of a portion of the eastern seaboard of the United States, centered on the city of Philadelphia.

Figure 13 Enlargement of the New York City subimage area in Fig. 11.



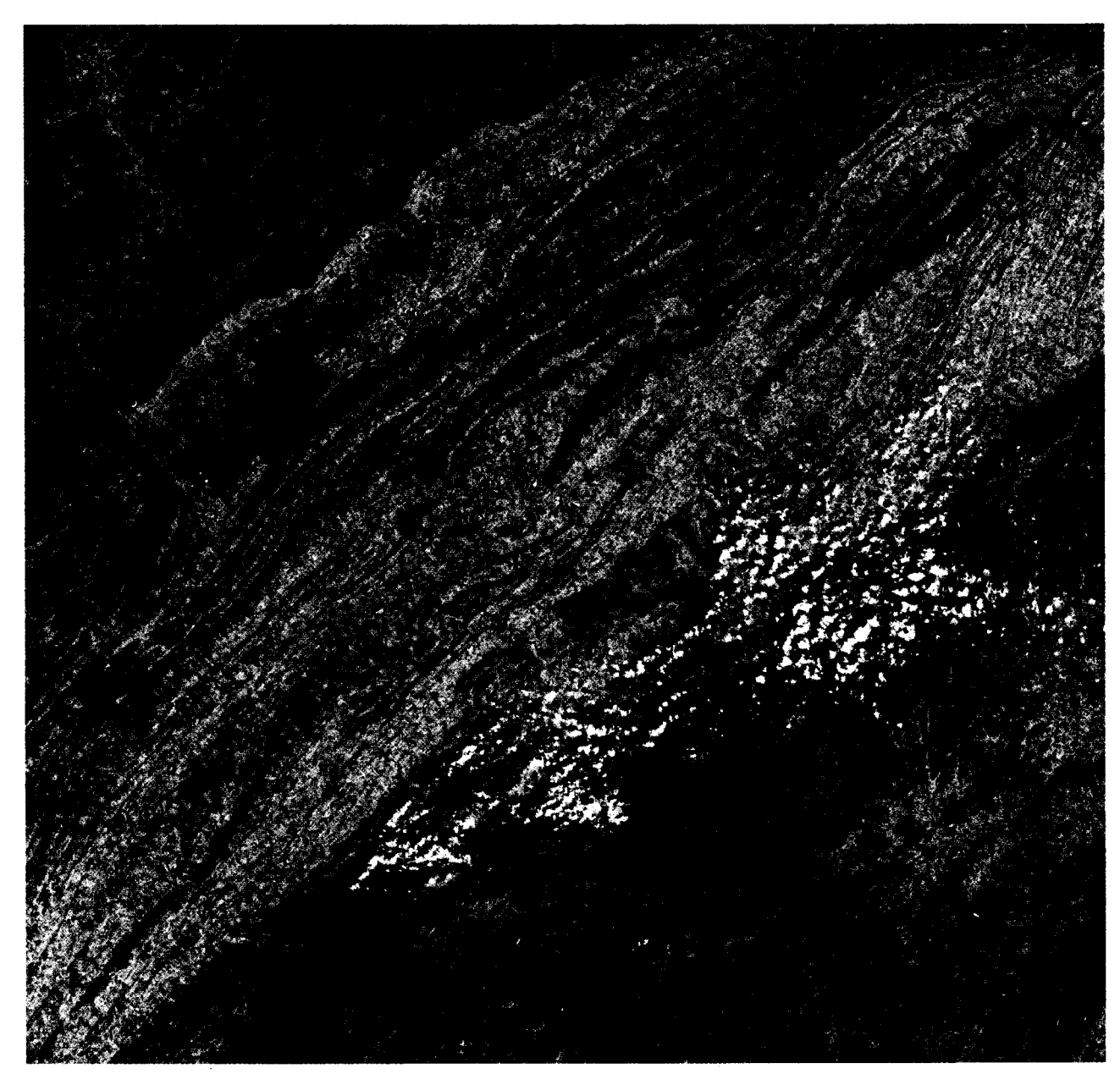


Figure 14 Color composite (bands 4, 5, and 7) of the Tennessee valley region around Knoxville.

edge data but, because the radiometric distortion is extreme near the edges, zero-order extrapolation proved to yield the best results [12].

With the inclusion of edge values, these computations finally produce 20×20 arrays of gain and bias values which completely span the image. The values can be fit in a least-square-error sense with spatially dependent functions G(x, y) and B(x, y). For this, it is computationally efficient to divide the image into zones, within which constant values of G and B can be used with an acceptably small error.

Digital image processing results

A number of Multispectral Scanner and Return Beam Vidicon scenes have been processed by these correction elements. In this section we present some of the results in both numerical and pictorial form.

• Geometric correction

It was found that for MSS data the number, distribution, and registration accuracy of GCPs influence the accuracy of the output image data. Figure 7 shows the root-mean-square distance error as a function of the number of

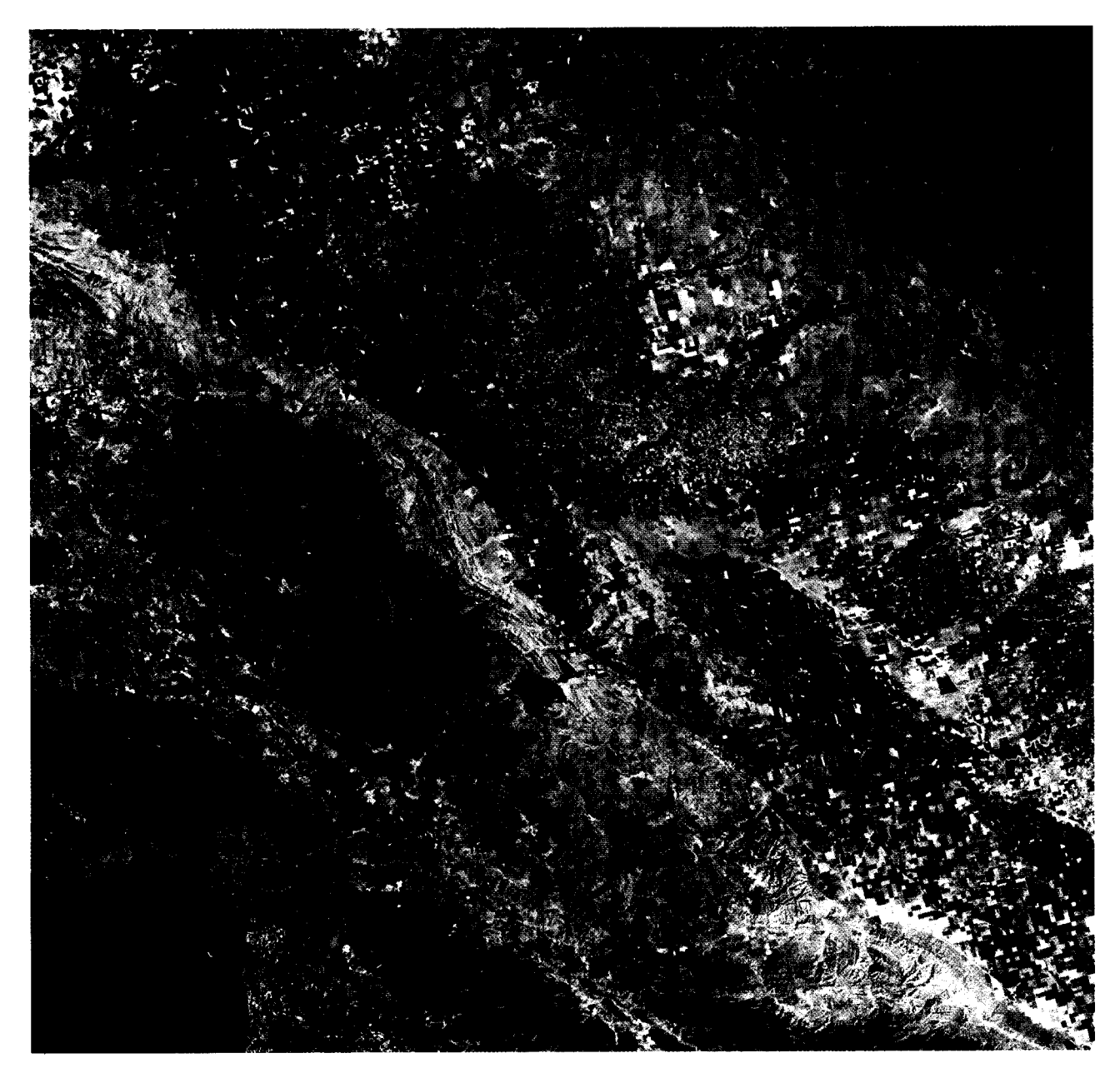


Figure 15 Color composite (bands 4, 5, and 7) of the central California area also shown in Fig. 8; Monterey Bay is at the lower left.

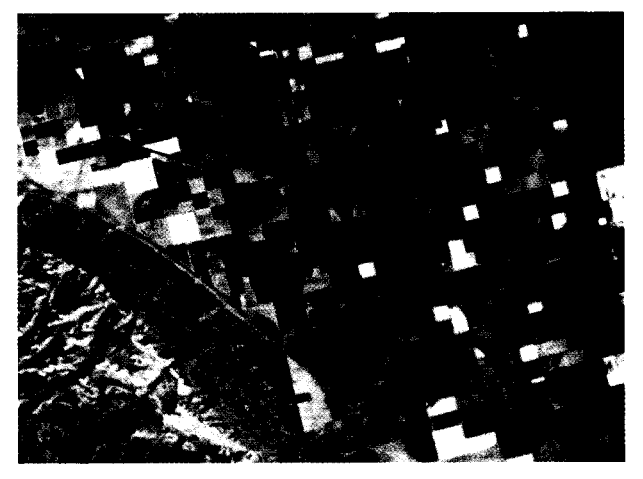


Figure 16 Representational-color composite subimage of the San Joaquin valley showing agricultural features: red—alfalfa and other healthy green crops; orange—safflower; light yellow—barley; blue-green—fallow fields; blue—water; and black—barley fields recently harvested (and burned over).

51

GCPs, from a well distributed set, used to establish the distortion characteristics of a scene; 16 seems to be a reasonable number of GCPs to use for an acceptable degree of accuracy.

The relative geometric accuracy of the processed image data is determined by comparing the positions of picture elements in the processed GCP scene with U.S. Geological Survey maps, with translation errors removed, through the use of metric functions to determine similarity. Table 6 is a summary of the typical accuracy obtained; for 90 percent of the GCPs, a relative geometric accuracy of about one picture element (79 m) can be achieved. (The use of the 90-percent figure is consistent with a National Map Accuracy Standard for error measurement.)

Figures 8(a) and (b) are MSS images of a central California area before and after correction. The "before" image is a rectangle because of the overlapping of the along-scan sample values (1.4:1 oversampling) and because no Earth rotation correction has yet been made. The "after" image has been fully corrected and can be used as a map product at a scale of about 1:250000.

A similar geometric error analysis was made on corrected RBV data. Since each band corresponds to an independent sensor, an error value was determined for each band. Relatively high accuracy can be obtained with few GCPs because the sensor data are essentially independent of the satellite attitude rate (an RBV scene is imaged in 4 to 16 ms).

• Radiometric enhancement

Figure 8(c) shows an MSS image of the central California area with normal radiometric processing. Figures 8(d) and (e) show subimages after radiometric enhancement. Generally, in the infrared band, water appears black because of the low radiance response of water in the 0.8 to 1.1 µm wavelength range. A radiometric "stretching" operation was done on the water data, Fig. 8(e), to determine whether any additional information could be extracted for the Monterey Bay region. In addition, the area of San Jose north of Monterey Bay was processed to enhance the road network, Fig. 8(d). It is apparent that the radiometrically modified images exhibit information that would not have been normally detected. These examples demonstrate that digital sensor data have a wider dynamic range than photographic film can provide. We estimate that twice the film range exists in the sensor data and that the additional information can be extracted by simple radiometric processing.

Three RBV bands were radiometrically corrected and the results, in terms of the number of zones, i.e., individual correction tables for each band, are given in Table 7.

Figures 8(f) and (g) show the RBV image of the same central California area before and after radiometric

correction. Most of the shading (non-uniform RBV response characteristic) has been removed, with the recovery of a significant amount of data.

◆ Temporal registration experiment

In some applications it is useful to have two or more images in geometric conformance, i.e., in registration with each other. This is particularly useful in change detection applications where a difference in ground features is of interest, such as shoreline erosion. In agricultural feature extraction applications, the use of multiple scenes of the same area over a crop maturation period improves crop classification accuracy. For these types of applications, extremely precise geometric correction of the various scenes must be made so that corresponding ground features of both scenes are assigned the same geographic location and are thus in conformance.

An experiment was conducted to determine the geometric similarity of two digitally processed scenes. A scene that included Phoenix, Arizona was processed (using 20 GCPs) to correct all geometric errors; this served as a reference image. Then a scene, acquired 36 days later, was processed using the earlier scene as a geometric ground control reference. Both processed scenes were recorded on film and are shown in Fig. 9.

To evaluate relative error, 69 features were located in each scene and the differences in corresponding line and sample coordinates were computed. The results showed temporal registration errors less than 0.24 picture element in sample location and less than 0.11 picture element in line location for 90 percent of the features. When the scene transparencies are overlaid, no geometric difference can be discerned. This experiment demonstrates that multiple scenes can be corrected to be in conformance within about one-fourth picture element.

Mosaicking

Techniques have been developed to digitally combine two or more scenes [19]. The object of mosaicking is to allow a larger area to be viewed; e.g., some geologic faults or lineaments and some hydrologic features are thousands of kilometers in length. By combining multiple scenes with precise correction, information extraction can be improved. Figure 10 shows a circular geologic feature that was recorded midway between two scenes; its unusual shape was not evident before the scenes were mosaicked.

Figure 11 is a digital mosaic of a portion of the east coast of the United States. This mosaic was produced by merging three contiguous MSS scenes and geometrically correcting the swath. No geometric discontinuity is apparent in the processed scene. Bands 4, 5, and 7 have been combined into a representational-color composite

"photograph" in which, for example, vegetation is shown in red.

Reference 20 contains a digital mosaic of a Montana-Wyoming region, produced from eight MSS scenes. Those scenes were acquired 24 hours apart and were digitally mosaicked to produce one composite image. First, the scenes of the first swath were merged and geometrically corrected. Next, the scenes of the second swath were merged and corrected, so that common GCPs were in coincidence. Finally, the overlapped region was removed from one swath and the two swaths were combined.

Figure 12 is a digital mosaic of the entire United States, produced from infrared and visible light sensor data (0.4 to 1.0 μ m) accumulated on three nighttime south-to-north passes of a meteorological satellite at an altitude of 835 km. Each sweep provided ground coverage of a 3000-km wide swath but, because of the wide (112°) field of view, the sensor data contained severe panoramic distortion. Geometric correction programs were used to eliminate this distortion and to convert the data to a Lambert conformal conic projection. The data from the three swaths were then adjusted for intensity variations and mosaicked into the scene shown. Los Angeles, San Francisco, Seattle, and other cities outline the west coast; Miami, Washington, Philadelphia, New York and other cities can be identified on the east coast (clouds obscured Boston and other northern cities); and most medium-to-large cities in the interior of the United States can also be identified.

Enlargement

An image can be enlarged by a number of digital techniques. One involves simple picture element and line repeating, which enlarges an image by an integral factor. If the enlargement factor is too great, however, the image may have the appearance of discrete blocks. Resampling of the data can enlarge an image without this effect. Figure 13 shows a subimage area, centered on New York City in Fig. 11, which has been digitally enlarged using a cubic convolution resampling function. Note that great detail can be resolved despite the fact that the sensors were at an altitude of 500 nautical miles (915 km).

• Information extraction

Figure 14 is a digitally processed color composite scene of the southwest-northeast valley region of Tennessee between the Cumberland and the Great Smoky Mountains. Numerous intricate land-water interfaces are visible, e.g., the serpentine Douglas Lake near the center, which was formed by the dam at its western end, and Cherokee Lake, north of Douglas Lake, also formed by a dam at its western end. Digitally processed images such as this are used to monitor the condition of lakes,

predict and assess flood damage, anticipate irrigation requirements, and develop hydrologic models for water management.

In Fig. 14, as well as in the other color composite illustrations in this paper, although water is represented by a medium-to-dark blue color, which appears "natural" to the human eye, this color is actually a representational one based on integration of digitally recorded information from two wavelength bands in the visible range (bands 4 and 5) and one band (7) in the infrared region, which is not perceived by the eye. In this system, urbanized areas such as Kingsport, Tennessee, at the upper right and Knoxville, west of Douglas Lake, are generally represented by a light blue color (which in part indicates the infrared reflectivity of asphalt roads and roofs).

Figure 15 is a color composite of the central California scene in Fig. 8. This image was also produced by photographic combination of digitally processed bands 4, 5, and 7. Of significance are the agricultural, geologic, hydrologic, and urban features that are readily discerned. For example, the San Andreas fault, with a northwestsoutheast orientation, can be seen at the lower left, and the Diablo Mountain ranges are easily identifiable. Crops in the San Joaquin valley, including alfalfa, barley, rice, and safflower, can be identified visually by color (see the agricultural subimage in Fig. 16) and can be accurately and rapidly classified by computer processing. Such computer-programmed spectral classification has achieved crop identification and area determination accuracy as high as 98 percent. Also visible in this scene are reservoirs (the San Luis reservoir is in the center) and irrigation canals and aqueducts leading from the San Luis reservoir. Various urban areas in central California such as San Jose, Merced, and Salinas are quite apparent, and this kind of data is often useful to land-use planners.

An MSS scene of the northwestern part of Pakistan was used in a mineral exploration experiment [8] by U.S. scientists in cooperation with Pakistani government agencies to seek previously undiscovered mineral deposits using multispectral classification techniques. Digital image data for a known copper-bearing region were used in a pattern-recognition program to identify similar rock and surficial materials generally associated with subsurface copper ore, and five previously unknown mineral-rich areas were discovered. The Pakistan scene is reproduced in Ref. 20.

Computer configurations and analysis

Our image processing program development and experimentation were performed at the Gaithersburg image processing facility. This facility consists of a general

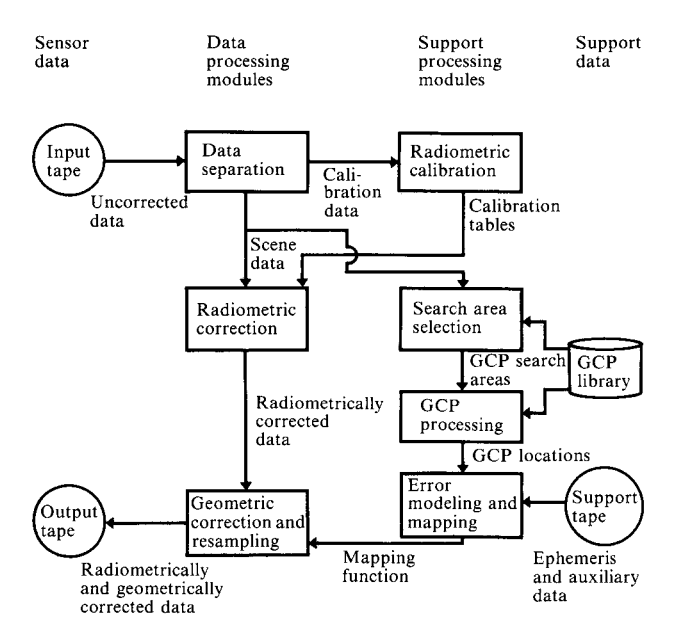


Figure 17 Image processing operations and associated data flow.

purpose computer, an interactive image display system, a variety of application software, and image recorders [20].

An image processing configuration analysis addressed the requirements of an operational environment, i.e., the processing of multiple Landsat scenes on a production basis. Figure 17 is a schematic of the image processing operations and the associated data flow.

Several general purpose computer configurations and one special purpose configuration were analyzed in an implementation of the image processing algorithms. Several system configurations were considered and their performance evaluation was predicted through the use of analytical models [12]. For each, the following processing steps were considered:

Step 1

Input image data are read from magnetic tape and transformed to a pixel-interleaved (by band) format.

Supporting data (e.g., ephemeris) are read.

Image data are radiometrically corrected by table-lookup.

Table 8 Configuration definitions.

Configuration	Reformatting and Input radiometric tape correction guration type processor		Geometric correction processor	Geometric correction function	Output tape type
A	800-BPI ^a CCT ^b	One GPP ^c		Individual scene	6250-BPI CCT
В	$\mathbf{HDDT}^{\mathrm{d}}$	One GPP		Individual scene	6250-BPI CCT
С	HDDT	One microprogrammed SPP ^e	One GPP	Individual scene	6250-BPI CCT
D	HDDT	One SPP	One GPP	Entire pass for MSS; individual scene for RBV	HDDT
Е	HDDT	One SPP	One SPP supported by one GPP	Entire pass for MSS; individual scene for RBV	HDDT

aBPI:

Bits(s)-per-inch

^dHDDT: High density digital tape ^eSPP: Special purpose processor

^bCCT: Computer-compatible tape ^cGPP: General purpose processor

tape ^eSPP:

Table 9 Scene throughput summary (in scenes processed per 12-hour day).

Configuration	IBM System/ 370 Model														
	135		145		155		158		168						
	MSS	RBV	Both	MSS	RBV	Both	MSS	RBV	Both	MSS	RBV	Both	MSS	RBV	Both
Α	25	14	9	43	23	15	86	48	31	107	59	38	141	74	48
В	25	14	9	43	23	15	94	48	32	153	69	48	400	180	124
С	44	34	19	68	54	30	144	93	56	211	118	75	400	200	133
D	64	36	23	94	57	35	211	110	72	313	146	100	720	300	211
E ^a	194	40	33	313	64	53	514	126	101	654	175	138	1200	450	327

54

aWith and without laser beam recorder,

Ground Control Point (GCP) and reseau search areas (as required) are extracted from the input stream and stored for subsequent detection operations.

Step 2

GCPs are located in the image data.

Reseau (for RBV images only) are located in the image data.

Geometric correction functions are generated.

Step 3

Geometric corrections are applied using different techniques.

Corrected, annotated data are written on magnetic tape in picture-element-interleaved format.

Step 4

User-requested scenes are selected from the master output tape and copied onto user tapes.

The five computer configurations considered are defined in Table 8, which summarizes the assumed processing requirements and environment. Two alternative I/O media were assumed—computer-compatible tape and high density digital tape. For the highest-throughput configuration (E), a variation including direct film output to a laser beam recorder was also evaluated. The detailed configurations and analysis can be found in Ref. 12.

A summary of the results of the configuration analysis is given in Table 9. Throughput figures are in scenes per day (a scene consists of all spectral band images of a 185-km × 185-km area). Many throughput figures are much larger than the daily processing requirement anticipated but are listed as a measure of the computing capacity available for other tasks, for example, production of user tapes. The smaller general purpose processors are CPU-bound, but the use of an attached, microprogrammed, special purpose processor and the use of high density digital tape were found to significantly increase system throughput.

Conclusions

Several conclusions can be drawn from the work that has been performed:

Utility Because of the digital nature of advanced sensors, and information extraction techniques that use digital computers, it is advantageous to correct sensor data using digital rather than electro-optical techniques. Corrected sensor data can be generated with no data degradation, resulting in improved information extraction.

Accuracy Digital correction of digital sensor data results in geometric errors of less than one picture element and in full preservation of sensor radiometry. No radiometric error or loss is introduced (as occurs in electro-optical processing with its data conversions and multiple photographic generations).

Throughput Production image processing systems can be configured to allow high speed processing of Earth observation data. Microprogrammed signal processors can be used to improve the cost/performance ratio relative to conventional general purpose computer configurations, where high throughput systems are required.

Flexibility Digital processing provides a significant degree of processing and operational flexibility. Correction, enhancement, mosaicking, and information extraction can all be done with the same hardware by sequential selection of software routines.

Feasible technology In the past, the use of digital technology and, in particular, digital computers for image processing, was considered impractical because the parallel nature of the data conflicted with the serial nature of digital processors. However, advanced sensors provide serial digital data, and advanced digital hardware provides parallel processing capability. This inversion of organization, combined with high speed circuitry and efficient algorithms, has made a major impact on image processing technology. It is likely that most future ground systems for processing Earth observation data will use digital technology and techniques.

Acknowledgments

The significant contributions of M. L. Cain, C. P. Colby, R. D. Depew, D. G. Ferneyhough, T. Gaidelis, S. W. Murphrey, C. W. Niblack, J. J. Przybocki, and H. Silverman to the research, analysis, programming, and film processing described in this paper are gratefully acknowledged. The basic concepts of reseau detection and image processing were suggested by R. Bakis, M. A. Wesley, and P. M. Will. The support and encouragement of the National Aeronautics and Space Administration was instrumental in implementing this work, which was partially funded by NASA contract NAS5-21716.

Appendix: Derivation of cubic convolution resampling filter

It can be shown that a band-limited sampled signal can be reconstructed (resampled) without information loss by the use of a filter which, in one dimension, has the form

$$I(x_j) = \sum_k I(x_k) f(x_j - x_k), \tag{A1}$$

where $I(x_k)$ is the input signal being reconstructed, x_k is the picture element location of the input signal, and f(x) is the reconstruction filter.

Ideally, a reconstruction filter of the form $f(x) = \sin x/x$ should be used. This function, however, requires an infinite amount of data. The use of an equivalent digital filter operator requires an infinite number of input signal terms, due to the continuous nature of the operator.

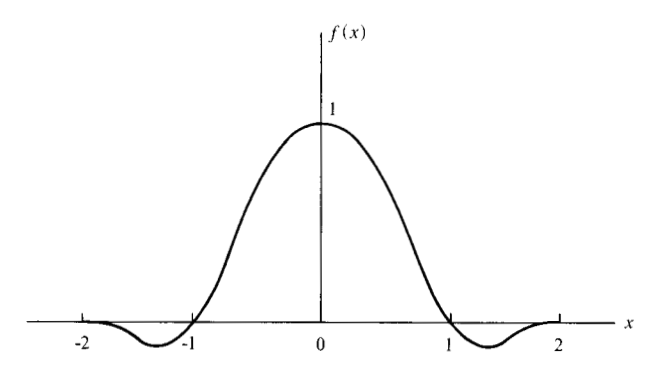


Figure A1 Approximation of $\sin x/x$ resampling function used in cubic convolution

An approximation of f(x), shown in Fig. A1, is desirable. No term beyond x = 2 exists. This form reduces the input data requirement to four values (one dimension) or sixteen (two dimensions).

Such a filter can be developed as a cubic spline curve

$$f(x) = \begin{cases} f_1(x) = a_1 |x|^3 + b_1 |x|^2 + c_1 |x| + d_1, \ 0 \le |x| < 1; \\ f_2(x) = a_2 |x|^3 + b_2 |x|^2 + c_2 |x| + d_2, \ 1 \le |x| < 2; \\ f_3(x) = 0, \ 2 \le |x|. \end{cases}$$
(A2)

The conditions used [18] to approximate $\sin x/x$, cubic convolution, are slope and value continuity, symmetry about x = 0, and a cutoff value. Further, the resampling function should have a value of one at the center and zero at all other points separated from the center by an integral multiple of the sampling interval.

The functions obtained under these constraints are

$$f_1(x) = (a_2 + 2)|x|^3 - (a_2 + 3)|x|^2 + 1;$$

$$f_2(x) = a_2|x|^3 - 5a_2|x|^2 + 8a_2|x| - 4a_2.$$
 (A3)

Bounds on the value of a_2 can be obtained by requiring that f_2 be concave upward at |x| = 1, and f_1 be concave downward at x = 0. Thus

$$\frac{d^2}{dx^2} f_2(x)|_{x=1} = -4a_2 > 0 \to a_2 < 0; \tag{A4}$$

$$\frac{d^2}{dx^2} f_1(x)|_{x=0} = -2(a_2 + 3) < 0 \to a_2 > -3.$$
 (A5)

With $a_9 = -1$, as in [18], the coefficients determined above produce the cubic convolution polynomial

$$f(x) = \begin{cases} f_1(x) = 1 - 2|x|^2 + |x|^2 + |x|^3, \ 0 \le |x| < 1; \\ f_2(x) = 4 - 8|x| + 5|x|^2 - |x|^3, \ 1 \le |x| < 2; \\ f_3(x) = 0, \ 2 \le |x|. \end{cases}$$
 (A6)

This function is the one plotted in Fig. A1.

References

- 1. E. P. Mercanti, "ERTS-1, Teaching Us a New Way to See," Astronautics & Aeronautics Vol. 11 26
- 2. J. C. Fletcher, "ERTS-1, Toward Global Monitoring," Astronautics & Aeronautics, Vol. 11, p. 32, September 1973.
- 3. Proceedings of the Symposium on Significant Results Obtained from the Earth Resources Technology Satellite-1, March 1973, Vol. I, Section B, NASA SP-327, compiled and edited by S. C. Freden, E. P. Mercanti, and M. A. Becker, NASA Goddard Space Flight Center, Greenbelt, Maryland.
- Proceedings of the Third Earth Resources Technology Satellite-1 Symposium, December 1973, NASA SP-351, compiled and edited by S. C. Freden, E. P. Mercanti, and M. A. Becker, NASA Goddard Space Flight Center, Greenbelt, Maryland.
- 5. G. Bylinsky, "ERTS Puts the Whole Earth Under a Microscope," Fortune Magazine, Vol. XCI, p. 117, February
- 6. Abstracts of the NASA Earth Resources Survey Symposium, June 1975, NASA Johnson Space Center, Houston,
- 7. R. B. MacDonald, F. G. Hall, and R. B. Erb, "The Use of LANDSAT Data in a Large Area Crop Inventory Experiment (LACIE)," Proceedings of the NASA Earth Resources Survey Symposium, June 1975, NASA Johnson Space Center, Houston, Texas.
- 8. R. G. Schmidt, B. B. Clark, and R. Bernstein, "A Search for Sulfide-Bearing Areas Using LANDSAT-1 Data and Digital Image-Processing Techniques," Proceedings of the NASA Earth Resources Survey Symposium, June 1975, NASA Johnson Space Center, Houston, Texas.
- 9. ERTS Data Users Handbook, NASA 715D4249, NASA Goddard Space Flight Center, Greenbelt, Maryland.
- 10. R. Bernstein, "Results of Precision Processing (Scene Correction) of ERTS-1 Images Using Digital Image Processing Techniques," Proceedings of the Symposium on Significant Results Obtained from the Earth Resources Technology Satellite-1, March 1973, Vol. I, Section B, NASA SP-327, NASA Goddard Space Flight Center, Greenbelt, Maryland.
- 11. R. Bernstein, "Scene Correction (Precision Processing) of ERTS Sensor Data Using Digital Image Processing Techniques," Proceedings of the Third Earth Resources Technology Satellite-1 Symposium, December 1973, Vol. I, Section B, NASA SP-351, NASA Goddard Space Flight Center, Greenbelt, Maryland.
- 12. R. Bernstein, "All-Digital Precision Processing of ERTS Images," IBM Final Report to NASA, Contract NAS5-21716, April 1975, NASA Goddard Space Flight Center, Greenbelt, Maryland.
- 13. R. H. Kidd and R. H. Wolfe, "Performance Modeling of Earth Resources Remote Sensors," IBM J. Res. Develop. 20, 29 (1976, this issue).
- 14. D. T. Barnea and H. Silverman, "A Class of Algorithms for Fast Digital Image Registration," IEEE Trans. Computers C-21, 179 (1972).
- 15. R. Bernstein and H. Silverman, "Digital Techniques for Earth Resources Image Data Processing," Proceedings of the American Institute of Aeronautics and Astronautics, 8th Annual Meeting and Technology Display, Washington, D.C., October 1971, Vol. C21, No. 2, AIAA 71-978, New York, N.Y.
- R. Fletcher and M. I. D. Powell, "Rapidly Convergent Descent Methods for Minimizing," Computer J. 6, 163 (1963)
- 17. H. Markarian, R. Bernstein, D. G. Ferneyhough, L. E. Gregg, and F. S. Sharp, "Digital Correction for High-Resolution Images," *Photogrammetric Engineering and Re*mote Sensing (J. Am. Soc. Photogrammetry) 39, 1311 (1973).

- S. S. Rifman and D. M. McKinnon, "Evaluation of Digital Correction Techniques for ERTS Images," TRW Corporation Final Report, TRW 20634-6003-TU-00, NASA Goddard Space Flight Center, Greenbelt, Maryland, March 1974.
- "Feasibility of Generating Mosaics Directly from ERTS-1 Digital Data," IBM Final Report to U.S. Department of the Interior, Contract 08550-CT3-12, TR FSC72-0140, IBM Federal Systems Division, Gaithersburg, Maryland, April 30, 1974.
- 20. R. Bernstein and D. G. Ferneyhough, "Digital Image Processing System," *Photogrammetric Engineering and Remote Sensing (J. Am. Soc. Photogrammetry)* 41, 1465 (1975).

Received April 16, 1975; revised September 19, 1975

The author is with the IBM Federal Systems Division, 18100 Frederick Pike, Gaithersburg, Maryland 20760.

Erratum

Figure 6 in "Digital Image Processing of Earth Observation Sensor Data" (R. Bernstein, *IBM J. Res. Develop.*, Vol. 20, p. 40, January 1976) was mislabeled. The correct sequence of subimages proceeds counterclockwise from (a); i.e., (c) becomes (b), (d) becomes (c), and (b) becomes (d)